Astron. Astrophys. 323, 217–222 (1997)

ASTRONOMY AND ASTROPHYSICS

NGC 7027: discovery of a Raman line in a planetary nebula⋆

D. Péquignot[1], J.-P. Baluteau[2], C. Morisset[1], and C. Boisson[1]

[1]Laboratoire d'Astrophysique Extragalactique et de Cosmologie associé au CNRS (URA 173) et à l'Université Paris 7, DAEC, Observatoire de Paris-Meudon F-92195 Meudon Cédex, France
[2]Laboratoire d'Astronomie Spatiale, LP CNRS, BP 8, F-13376 Marseille Cédex 12, France
(pequignot@obspm.fr, baluteau@astrsp-mrs.fr, morisset@obspm.fr, boisson@obspm.fr)

Received 28 November 1996 / Accepted 16 December 1996

Abstract. We report on the discovery of the He II Raman line λ 485.1 nm in the spectrum of the planetary nebula NGC 7027.

This line is direct evidence for the presence of atomic hydrogen in the nebula.

It is shown that this Raman line can provide reliable pieces of information concerning both the velocity field of the He^{2+} region and the expansion velocity of the surrounding H^0 shell.

Detection of self-Raman scattering of Ly_γ is suspected.

Key words: atomic processes – line: identification – line: profiles – ISM: general – ISM: planetary nebulae: general – ISM: planetary nebulae: individual: NGC 7027

1. Introduction

Schmid (1989) solved elegantly the longstanding problem of identifying a pair of broad emission lines $\lambda\lambda$ 682.5, 708.2 nm, which frequently appeared in the spectrum of symbiotic binaries. Schmid showed that all known properties of these lines could be understood as a consequence of Raman scattering of O VI 103.2, 103.6 by neutral hydrogen.

In this process a photon is captured from $H^0(1s)$ into an intermediate state which promptly decays onto an ns or nd level. The elastic case, in which the atom decays back to its ground state $1s$, corresponds to Rayleigh scattering.

The Raman-scattering cross section of $H^0(1s)$ strongly peaks at the resonance energies corresponding to the Lyman lines. Therefore favourable conditions for detecting Raman lines are (i) strong lines with wavelengths near Lyman wavelengths and (ii) an H^0 region with large column density.

Symbiotic binaries consist of a red giant star and a hot compact companion. The atmosphere and the inner wind of the cool star provide plenty of atomic hydrogen to Raman/Rayleigh scatter line radiation from the hot star and its highly ionized neighbourhood.

Nussbaumer et al. (1989), Isliker et al. (1989), Schmid (1992), Schild & Schmid (1996), and references therein illustrated diagnostic possibilities of theses lines. Meanwhile van Groningen (1993) provided further evidence for Raman scattering: in one symbiotic, RR Telescopii, he detected Raman scattered He II $(2-8)$ and He II $(2-10)$ at λ485.1 nm and λ433.3 nm.

To date, Raman lines have only been considered for symbiotic stars. Nonetheless the H^+ region of the high-excitation planetary nebula NGC 7027 is surrounded by a large molecular cloud discovered by Mufson et al. (1975) (e.g., Jaminet et al., 1991) so that an H^0 region is expected to exist at the interface (e.g., Graham et al., 1993).

Here we report on the discovery of the Raman line He II 485.1 in NGC 7027 and draw some consequences. A preliminary account was presented by Péquignot et al. (1996).

2. Raman wavelengths

The Raman scattering of He II $(2-n)$ by H^0 is sketched in the H I Grotrian diagram of Fig. 1, assuming for example $n = 8$. A Balmer photon ν_{HeII} of He^+ is captured into an intermediate state (dashed segment close to $4p$) which can promptly decay to either state $1s$ (Rayleigh-scattered UV photon with $\nu_{Ray} = \nu_{HeII}$) or state $2s$ (Raman-scattered optical photon with $\nu^B_{Ram} = \nu_{HeII} - E(2s)/h$), or else one of the states $3s$ and $3p$ (Raman-scattered near-infrared photon with $\nu^P_{Ram} = \nu_{HeII} - E(3s)/h$ and $\nu^P_{Ram} = \nu_{HeII} - E(3d)/h$).

Since there exists a continuum of intermediate states, the width $\Delta\nu_{HeII}$ of the initial line is conserved by Raman scattering so that the *relative* width $\Delta\nu^B_{Ram}/\nu^B_{Ram} = \Delta\lambda^B_{Ram}/\lambda^B_{Ram}$ is $\lambda^B_{Ram}/\lambda_{HeII}$ times that of the initial line. In a case of simple Doppler broadening, $\Delta\lambda/\lambda$ is about the same at all wavelengths and the Raman lines will appear anomalously broad (e.g., Schmid, 1989). Any wavelength shift in the rest frame of the scattering atom will be amplified in a similar manner.

Send offprint requests to: D. Péquignot

⋆ Based on observations performed at Observatoire de Haute-Provence, France.

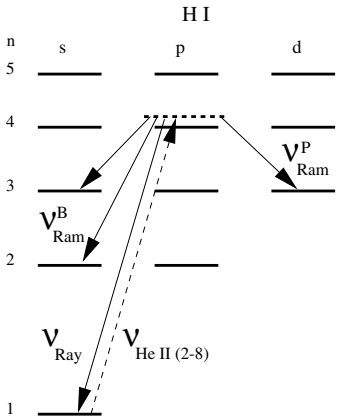

Fig. 1. Raman scattering of He II $(2-8)$ by H I. Notations as in the text.

Table 1. Raman components corresponding to He II $(2-8)$

λ (nm)	relative I	λ (nm)	relative I
484.997	0.4462	485.134	0.8033
484.999	0.0537	485.135	0.0892
485.008	0.5192	485.137	0.1075
485.010	0.2595	-	-
short λ^B_{Ram}:		long λ^B_{Ram}:	
485.004[a]	1.2786	485.135[a]	1.0000

[a] weighted mean $\overline{\lambda^B_{Ram}}$ = 485.0616 nm.

The wavelengths of the He II Raman lines can be computed from the H I and He II level energies tabulated by Garcia & Mack (1965) and corrected for air refraction (Allen, 1973). The wavelengths of the 7 individual components corresponding to transitions He II $(2-8)$ are listed in col. 1 and col. 3 of Table 1.

The relative intensities of the 7 components were derived from the radiative transition probabilities A_{ij} obtained by Green et al. (1957) and the "departure coefficients" b_{nl} obtained by Storey & Hummer (1995) assuming case B recombination. Results appear in col. 2 and col. 4 of Table 1 for T = 1.5×10^4 K, $n_e = 10^4$ cm^{-3}. The relative intensities were found to be almost constant over the range of physical conditions met in usual nebulae.

The 7 wavelengths tend to cluster around two definite values (shorter and longer λ's in col. 1 and col. 3 of Table 1 respectively) and it will often be sufficient in practice to distinguish only two "mean" components (the short and long λ^B_{Ram}'s), whose wavelengths and relative intensities are given in the lower part of Table 1. A good approximation to the intensity ratio of the λ^B_{Ram}'s over a large range ot temperatures is $I_{485.00}/I_{485.13} = 1.279 \times (T/1.5 \times 10^4 \mathrm{K})^{0.058}$. The overall weighted mean rest wavelength is $\overline{\lambda^B_{Ram}}$ = 485.062 nm.

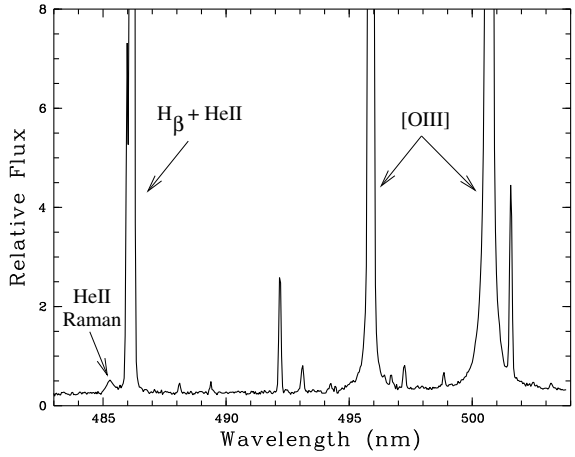

Fig. 2. The 483–504 nm spectrum of NGC 7027 (Five 180 s exposures co-added). The intensity of He II 485.93, blended with H_β, is about 2.9 % of I_β at the position observed. The broad feature in the blue wing of H_β is identified with the He II Raman line corresponding to He II $(2-8)$.

3. Observations

Spectra for the range 482.8–503.8 nm were obtained on 1995 August 1st at the 193 cm telescope of Observatoire de Haute-Provence (France) using the CARELEC spectrograph (Lemaitre et al., 1990) and a TK512 CCD.

The mean outer radius of the H^+ region of NGC 7027 is $4''$ (e.g., Masson, 1989) and absorption by local dust is unevenly distributed (e.g., Robberto et al., 1993). The seeing was $\sim 2.5''$. A $2.4''$ slit was oriented East-West across the brightest optical patch so that the South edge of the slit was going approximately through the centre of the nebula and the slit encompassed about 80% of the North half H^+ region.

Five 180 s, six 600 s, and three 2700 s exposures were secured at a grating dispersion of 1.7 nm/mm, corresponding to 0.0411 nm/px. The nebular lines were marginally resolved. In all cases the CCD was read perpendicularly to the dispersion. Data reduction, including flat fielding, cosmic-ray impact removal by appropriate medians, and sky subtraction, was performed using the standard MIDAS package. Wavelength calibration was done from well-known strong nebular lines so that wavelengths were obtained directly in the rest frame of the nebula. The nebular spectrum was taken over 6 columns of the CCD ($7.5''$).

Short-, intermediate-, and long-exposure spectra were co-added separately, producing three spectra of increasing signal-to-noise ratios. We checked that the three spectra were superimposable even in the wings of strong lines, except for leak from the peak of highly saturated lines.

Fig. 2 shows the spectrum obtained after co-adding the 180 s exposures. A broad feature is obvious in the blue wing of H_β. Such a feature is not seen in the [O III] line wings for whatever exposure time. In the long exposure, the core of H_β is saturated but no important leak to next pixels in the dispersion direction of the CCD is detected. The analysis of the broad

feature will be presented using the long-exposure spectrum, although all exposures were used.

4. Discussion

4.1. Identification of the He II Raman line λ485.1 nm

In most nebula spectra, the blue side of H_β is deprived of significant lines and no plausible identification as a blend of several lines or a broad di-electronic line could be found for the broad feature λ485.2 nm. On the other hand, the peak of the feature is just $\sim$ 0.17 nm redward of the expected mean rest wavelength $\overline{\lambda^B_{Ram}}$ of the He II Raman blend considered in Sect. 2. Since (i) a very distinct characteristic of Raman lines is their great width (Sect. 2) and, particularly, (ii) wavelength shifts are amplified by Raman scattering so that the wavelength difference may not imply unrealistically large velocity fields within the nebula (Sect. 4.5.2), we take the identification of the feature with the He II Raman line corresponding to He II (2 − 8) as secure.

Further confirmation would come from detecting other He II Raman lines at the expected wavelengths. Unfortunately these lines are either faint or blended, requiring elaborate treatments before claiming detection and getting quantitative results. Such an analysis is in progress and will be reported elsewhere (Péquignot et al., in preparation). We anticipate that other Raman lines have indeed probably been detected.

4.2. Profile for strong lines

In order to correct for the influence of the far wing of H_β on the Raman feature, a fit to the effective profile of strong lines ([O III] 500.7, [O III] 495.9, H_β, and He II 485.9) was looked for, using the functional form:

$$I_\lambda = A[e^{-|\frac{\lambda-\lambda_0}{a}|^2} + \sum B_i e^{-|\frac{\lambda-\lambda_0}{b_i}|^{\beta_i}}],$$

in which λ_0 was the rest wavelength of a given line, A its (unsaturated) peak intensity obtained from short exposures, and the sum a possible representation of the instrument scattering profile. The weak unsaturated lines indicated a = 0.063 nm, also adopted for the core of strong lines (given the instrumental FWHM of 2.1 px, this value of a corresponds to a mean expansion velocity of 21 km s^{-1}). In order to sample homogeneously the near and far wings of the lines, the sum was extended over four terms with β_i = 1.5, 1.0, 0.75, and 0.5. It turned out that the scattering profile could not be taken as strictly symmetrical and the coefficients B_i were allowed to split into B_{is} and B_{il} for the short- and long-wavelength scattering wings respectively. A fit to the [O III] line profiles was obtained using a strictly linear (almost horizontal) underlying continuum and the coefficients given in Table 2.

Note that the B's are much less than unity and the fact they are different introduces no significant discontinuity at $\lambda = \lambda_0$, especially as the central pixels of strong lines are useless in long-exposure spectra.

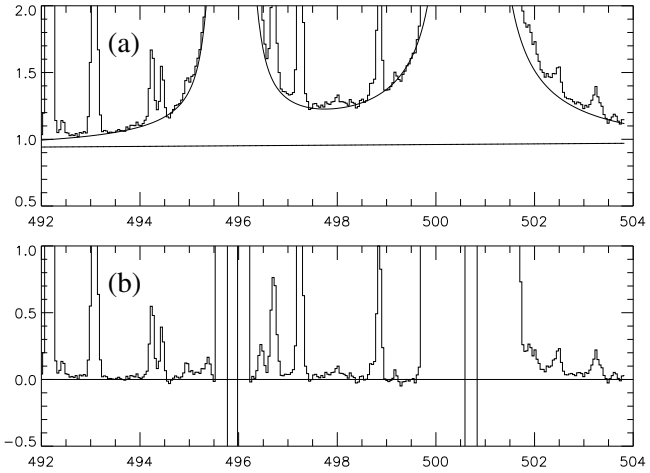

Fig. 3a and b. The 492–504 nm spectrum of NGC 7027 (Three 2700 s exposures co-added). In this and the subsequent figure, the vertical scale corresponds to a peak (unsaturated) intensity of 10^3 for H_β. **a** Upper part: the analytical fit to the instrument scattering profile for the [O III] lines superimposed on the original spectrum; the straight line is the continuum adopted over the full interval 483–504 nm. **b** Lower part: the residual spectrum after subtracting both the continuum and the [O III] line fit.

Table 2. Light-scattering profile coefficients

i	β_i	b_i (nm)	B_{is}	B_{il}
1	1.50	0.095	1.0×10^{-3}	9.0×10^{-3}
2	1.00	0.115	8.0×10^{-3}	5.0×10^{-3}
3	0.75	0.150	1.1×10^{-3}	1.0×10^{-3}
4	0.50	0.270	0.4×10^{-3}	0.4×10^{-3}

The 492–504 nm spectrum and the fit to the [O III] lines using the above parameters are shown in Fig. 3a for the long exposure. Fig. 3b illustrates that no [O III] line wing is left in the residual after subtracting the fit. The leakage of the strongly saturated [O III] lines and the effect of subtracting the gaussian cores of the lines are obvious in Fig. 3b. The description of the inner wings (larger β_i's) relied particularly on the 600 s spectrum, allowing to reduce the "blind" range to ± 0.04 nm about each of the [O III] lines (for example, the blend N II (19) 500.11 + 500.15 could be separated from [O III]). The same profile will be considered for H_β and He II 485.93 in Sect. 4.4.

4.3. Raman profile

A synthetic Raman profile was generated using the data of Table 1 and assuming the same velocity profile for all of the 7 original components He II (2 − 8). A factor $\lambda^B_{Ram}/\lambda_{HeII}$ = 4.99 was applied to the relative line widths before convolving with an instrumental profile taken as a gaussian of FWHM = 0.086 nm. From trial calculations it appeared that the global velocity profile for the He^{2+} emitting region could be neither a

triangle (too sharp at maximum), nor a gaussian (too gradual in the wings), nor a parabola (too steep in the wings). We therefore adopted a hyperbolic profile:

$$\frac{I}{I_m} = \frac{1 - [(v/v_0)^2 \times (1-\alpha^2) + \alpha^2]^{1/2}}{1-\alpha},$$

with I_m the maximum intensity (v = 0), $\pm$ v_0 the velocity at zero intensity, and α the "sharpness parameter" ($0 \leq \alpha < 1$; α = 0 corresponds to a triangle). With this profile, the mean expansion velocity varies from $1/2 \times v_0$ to $2/3 \times v_0$ for α varying from 0 to 1.

In order to make the theoretical and observed wavelengths of the Raman feature to coincide, a global velocity shift Δv had to be applied to the initial He II $(2-8)$ lines.

An implicit assumption in using the relative intensities of Table 1 is that the Raman conversion rate is independent of wavelength. This applies only in the limit of large Raman optical depth. In the optically thin case, the profile should be weighted by the Raman conversion efficiency, that is the Raman cross section σ, which varies almost exactly as the inverse square of the frequency shift from the H I $(1-4)$ Lyman line (e.g., Isliker et al., 1989). In the general case of a finite optical depth, the Raman conversion efficiency is taken as proportional to $1 - \exp(-\tau_m \times \sigma/\sigma_m)$, in which τ_m and σ_m are respectively the effective Raman optical depth and the Raman cross section corresponding to $\overline{\lambda^B_{Ram}}$.

Three fits were obtained assuming effective optical depths $\tau_m \ll, =, \gg 1$. With the assumed velocity profile, the blue side of the observed profile suggested τ_m of order unity or larger. In the following, an optical depth τ_m = 1 is adopted for illustration. Conclusions will not depend significantly on this choice.

4.4. Vicinity of H_β

The 483–489 nm spectrum is shown in Fig. 4a. The H_β and He II 485.93 profiles are modelled according to Sect. 4.2. To these model-lines is added the adopted synthetic Raman blend (assuming effective optical depth unity, Sect. 4.3 and 4.5.1). The continuum is as in Fig. 3a. The residual obtained after subtracting the synthetic profile from the original spectrum is shown in Fig. 4b.

The [O III] lines are much stronger than H_β and should provide a good template profile for the wings. Thus, although the fit to the innermost wings ($\pm$ 0.20 nm) of the H_β + He II 485.93 blend may be affected by saturation, leakage, and inexact description of the line profile, the wing subtraction should be reliable inasmuch as the properties of light scattering within the instrument are not changing too much from λ 486 nm to λ 496 nm.

In Fig. 4b, the dozen weak features with intensities $\sim 10^{-4} I_\beta$ or less are real and most of them could be identified (see captions to Fig. 4b: unidentified lines are noted "X"). In particular the top of the Raman feature is too sharp to be correctly modelled. The residual narrow feature turns out to be nicely identified with the line C III (6g–12h) 485.24, as confirmed by the presence of C III(6h–12i) 483.39 and C III (6^3f–12^3g) 487.64 at the correct wavelengths and with the correct relative intensities within uncertainties (lines obtained by extrapolation of known C^{2+} levels; see also Baluteau et al., 1995).

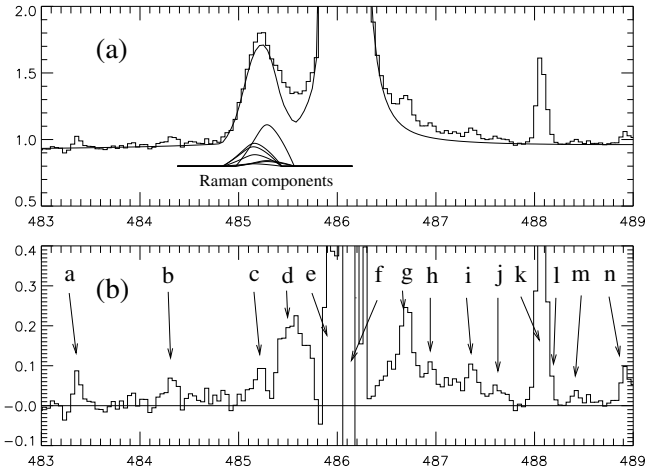

Fig. 4a and b. The 483–489 nm spectrum of NGC 7027 (Three 2700 s exposures co-added). **a** Upper part: the original spectrum together with the sum of (i) the analytical fit to the instrument scattering profile for H_β and He II 485.93 nm, (ii) the synthetic Raman-blend profile and (iii) the flat continuum. The insert shows the 7 Raman components on the same scale. **b** Lower part: the residual spectrum after subtracting the above fit (note the change of vertical scale). Line identifications: (a) C III (6g–12h) 483.39, (b) X 484.31 + O II (105) 484.34, (c) C III (6h–12i) 485.24, (d) X 485.6 broad (see text) + O II (29) 485.68, (e) N III (7) 485.88 + He II 485.93 subtracted, (f) H I 486.13 subtracted + N III (7) 486.13, (g) X 486.7 broad (see text) + N III (7) 486.71, (h) [F II] (1F) 486.93, (i) N III (7) 487.36, (j) C III (6^3f–12^3g) 487.64 + [Cr III] (3F) 487.75, (k) [Fe III] (2F) 488.10, (l) N III (7) 488.18, (m) N III (7) 488.41, and (n) X 488.90 + [Fe II] (4F) 488.96.

On the other hand, no convincing identification could be found for the relatively broad excess at λ485.4 – 485.7 nm (O II 485.68 $\sim$ 0.03 in the scale of Fig. 4; Liu et al., 1995). Since the H_β wings are in principle well described from the [O III] lines, we incline to consider this unexplained feature as real. Nonetheless this excess is too weak to seriously challenge either the identification or the proposed description of the Raman lines.

Rather than an imperfection of the fit to the Raman blend, the excess λ485.6 nm may be an independent feature. In fact a roughly similar feature is apparent on the other side of H_β at a symmetrical position and may therefore be of similar origin. The feature λ486.7 may look narrower than λ485.6, but this is probably due to the presence on its top of N III (7) 486.71, whose strength is of the order of that of N III 487.36 (Badnell, 1988). The dominant components of multiplet N III (7) are blended with H_β + He II. If the presence of the strong N III (7) 485.88 is at best suggested in Fig. 4b, several weaker components are detected (see captions to Fig. 4b).

The pair of features $\lambda\lambda$ 485.6, 486.7, as well as the probable shallow continuum excess to the red of λ 486.7 may reveal further Raman scattering of both the far wings of Ly_γ itself

and the underlying UV continuum, a process we can call "self-Raman scattering".

4.5. Velocity fields

4.5.1. Raman line profile

The fit to the Raman feature and the seven individual components are shown in Fig. 4a. Unlike the resulting blend, the components were drawn before convolving with the instrumental profile. Note that the components are distorted and their relative intensities are changed due to the varying efficiency of Raman conversion with wavelength (Sect. 4.3).

This fit was obtained assuming v_0 = 36 km s^{-1}, α = 0.2, and a velocity shift (to the red) Δv = +17.0 km s^{-1} for the original He II UV lines. Due to the "Raman broadening", the *apparent* values for the half width at zero intensity of the optical components and the global wavelength shift are 180 and 85 km s^{-1} respectively.

The derived parameters do not depend much on the assumed Raman optical depth, except for the velocity shift (Δv = 14.7 and 19.2 kms^{-1} for zero and infinite optical depths respectively).

Independent information about optical depth is needed in order to accurately determine the original velocity profile and the exact velocity shift. This should await measuring other He II Raman lines (Péquignot et al., in prep.).

With α = 0.2, the average expansion velocity we find for the He^{2+} shell is 0.556 $\times$ v_0 = 20.0 km s^{-1}, in good agreement with the high spectral resolution value of $\sim$ 19.8 km s^{-1} we estimate from the mean of the velocities for [Ne V] (19.1 km s^{-1}) and [O III] (20.4 km s^{-1}), as quoted by Osterbrock (1989).

The fact the parameter α is relatively small indicates that some material should be relatively slow in the local frame. Considering that little warm gas is believed to exist within an inner sphere of radius 2″ (e.g., Masson, 1989), the relatively large spread in He^{2+} velocity suggests that random turbulent motions largely in excess of the thermal velocity of helium ions should be added to the ordered radial motion (velocity proportional to the radius).

Alternatively α (and v_0?) may be somewhat larger, leaving a shallow excess continuum not unlike the one underlying the emission lines noted "h" and "i" in Fig. 4b.

4.5.2. Wavelength shift

The Raman feature is significantly redshifted relative to the rest wavelength for whatever Raman optical depth. According to our fit to the Raman profile, a typical velocity shift is 17 km s^{-1}, little dependent on the details of the assumptions (on general grounds, τ_m could hardly be very small or very large).

As long as the He^{2+} region is *globally* at rest in the rest frame of the system, that is no systematic motion in one priviledged direction exists (centrally symmetric expansion), the wavelength shift should originate in the scattering region.

In fact, as seen from any atom belonging to an expanding H^0 shell surrounding the He^{2+} zone, the *average* He II photon is produced in a region receding at the expansion velocity of the shell. Thus, ignoring to a first approximation possible effects of anisotropic scattering, the H^0 shell should expand at the velocity $\Delta v \sim$ 17 km s^{-1}. Quite interestingly, this value is intermediate between the expansion velocities for the bulk of the H$^+$ region, that is 21.2 km s^{-1}, as depicted from the H I lines (Osterbrock, 1989), and the bulk of the molecular cloud, that is 15.0 km s^{-1}, as depicted from the CO lines (Bieging et al., 1991).

4.6. Raman conversion efficiency

The maximum possible intensity $I^{max}_{485.1}$ of He II 485.1 will correspond to 100% Raman conversion of He II (2 − 8):

$$\frac{I^{max}_{485.1}}{I_\beta} = \frac{\epsilon_{HeII(2-8)}}{\epsilon_{HeII468.6}} \times \frac{I_{468.6}}{I_\beta} \times \frac{\lambda_{HeII(2-8)}}{\lambda^B_{Ram}} \times f^B_{Ram} \times C_{slit}$$

In this expression, the de-redenned intensity of He II 468.6 is 0.48 $\times$ I_β (Keyes et al., 1990), the ϵ's stand for the He II emissivities, taken from Storey & Hummer (1995) assuming case B recombination with T = 1.6 $\times$ 10^{4}K, n$_e$ = 6 $\times$ 10^{4}cm^{-3} (Gruenwald & Péquignot, 1989; Middlemass, 1990), f^B_{Ram} = 0.74 is the branching ratio for λ485.1, and finally C_{slit} is a factor correcting for the field of view of the spectrometer slit. Assuming spherical symmetry, the slit intercepts about 53% of half the H^0 region for any reasonable thickness of the H^0 shell and 80% of half the H$^+$ region so that $C_{slit} \sim$ 0.66. The resulting $I^{max}_{485.1}/I_\beta$ is 1.1 $\times$ 10^{-2}, that is $\sim$ 4 times larger than the observed intensity.

This is satisfactory in that it is not expected that all of the He II photons should be converted. Incomplete conversion may occur if (i) the effective Raman optical depth of the H^0 shell is relatively small, (ii) the H^0 shell is discontinuous (radiation leaking through holes), and (iii) competing mechanisms such as dust absorption are effective. Many combinations of these likely occurences are a priori possible. Information from other Raman lines is required before reaching definite conclusions.

Even though it may result from a combination of several parameters, the Raman conversion efficiency is an important probe of the H^0 region of a nebula. We note that, unlike for the O VI lines in symbiotics, the He II lines offer the possibility of a convenient and precise estimate of this efficiency since the intensity of the original UV recombination lines can be accurately determined from strong optical lines.

Despite the a priori more limited amount of H^0 available, the conversion efficiency of He II turns out to be much larger in NGC 7027 ($\sim$ 25%) than in symbiotic binaries (a few %). The main reason for this difference is probably geometry. In the case of symbiotics, the H^0 column density may be very large across the atmosphere of the giant star but the solid angle subtended by the star is necessarily quite small.

5. Concluding remarks

A broad emission feature λ485.2 detected in the spectrum of the planetary nebula NGC 7027 is identified as Raman scattered He II (2 − 8) by H I. This is the first detection of a Raman line in a nebula. The Raman conversion of He II is more efficient in NGC 7027 than in symbiotic stars.

A specific consequence of this detection is that other He II Raman lines should be observed in NGC 7027.

This observation provides the first direct evidence for the presence of H^0 in NGC 7027 since no 21 cm line detection has so far been reported (e.g., Taylor et al., 1990). It can be foreseen that the combined use of Raman scattering and 21 cm data will provide interesting constraints on the distribution of H^0 in nebulae.

The present analysis has demonstrated the value of low-dispersion spectroscopy of Raman lines as a tool to determine velocity fields in both the ionized and neutral regions of nebulae.

The discovery of a Raman line in a nebula opens the way to an entirely new kind of diagnostics for the neutral gas and the velocity fields in these objects.

Finally, as suggested by the present data, it is foreseen that a careful investigation of the H_β profile in nebulae will disclose the self-Raman scattering of Ly_γ.

References

Allen C.W., 1973, Astrophysical Quantities, 3rd edition, The Athlone Press (London)
Badnell N.R., 1988, J. Phys. B21, 749
Baluteau J.–P., Zavagno A., Morisset C., Péquignot D., 1995, A&A 303, 175
Bieging J.H., Wilner D., Thronson H.A. Jr., 1991, ApJ 379, 271
Garcia J.D., Mack J.E., 1965, J. Opt. Soc. Am. 55, 654
Graham J.R., Serabyn E., Herbst T.M., Matthews K., Neugebauer G., Soifer B.T., Wilson T.D., Beckwith S., 1993, AJ 105, 250
Green L.C., Rush P.P., Chandler C.D., 1957, ApJ Suppl. 3, 37
Gruenwald R.B., Péquignot D., 1989, IAU Symposium No. 131, Planetary nebulae, ed. S. Torres-Peimbert, Kluwer, Dordrecht, p. 224
Isliker H., Nussbaumer H., Vogel M., 1989, A&A 219, 271
Jaminet P.A., Danchi W.C., Sutton E.C., Russell A.P.G., Sandell G., Bieging J.H., Wilner D., 1991, ApJ 380, 461
Keyes C.D., Aller L.H., Feibelman W.A., 1990, PASP 102, 59
Lemaitre G., Kohler D., Lacroix D., et al., 1990, A&A 228, 546
Liu X.-W., Storey P.J., Barlow M.J., Clegg R.E.S., 1995, MNRAS 272, 369
Masson C.R., 1989, ApJ 336, 294
Middlemass D., 1990, MNRAS 244, 294
Nussbaumer H., Schmid H.M., Vogel M., 1989, A&A Lett. 211, L27
Osterbrock D.E., 1989, Astrophysics of Gaseous Nebulae and Active Galactic Nuclei, University Science Books (Mill Valley)
Péquignot D., Baluteau J.–P., Boisson C., Morisset C., 1996, IAU Symposium No. 180, Planetary nebulae, in press
Robberto M., Clampin M., Ligori S., Paresce F., Staude H.J., 1993, A&A 280, 241
Schmid H.M., 1989, A&A Lett. 211, L31
Schmid H.M., 1992, A&A 254, 224
Schild H., Schmid H.M., 1996, A&A 310, 211
Storey P.J., Hummer D.G., 1995, MNRAS 272, 41
Taylor A.R., Gussie G.T., Pottasch S.R., 1990, ApJ 351, 515
van Groningen E., 1993, MNRAS 264, 975

This article was processed by the author using Springer-Verlag LaTeX A&A style file *L-AA* version 3.